

Graphene-based Photodetector with Engineered Hot Carrier Cooling Dynamics

Yishu Huang^{1,2}, Anand Nivedan³, Florian Ludwig³, Bohai Liu⁴, Michiel Debaets^{1,2}, Steven Brems¹, Hai I. Wang⁵, Alessandro Principi⁶, Dries Van Thourhout^{1,2}, Christian Haffner¹, Aron W. Cummings³, and Klaas-Jan Tielrooij^{*4,3}

¹Imec, Kapeldreef 75, 3001 Leuven, Belgium

²Photonics Research Group, INTEC Department, Ghent University–imec, 9052 Ghent, Belgium

³Catalan Institute of Nanoscience and Nanotechnology (ICN2), CSIC and BIST, Campus UAB, Bellaterra, Barcelona 08193, Spain

⁴Department of Applied Physics, TU Eindhoven, Den Dolech 2, 5612 AZ Eindhoven, The Netherlands

⁵Debye Institute for Nanomaterials Science, Utrecht University, 3584 CS Utrecht, The Netherlands

⁶Department of Physics and Astronomy, The University of Manchester, Oxford Road, Manchester M13 9PL, United Kingdom

Abstract

Graphene has emerged as a promising material for integration into silicon photonics, owing to its ultrafast and broadband photoresponse without the need for an external bias voltage. This photoresponse relies on the photothermoelectric effect created by hot carriers. A key factor underlying the performance of graphene photodetectors is the cooling dynamics of these hot carriers. In this work, we engineer these dynamics in a WSe₂-graphene-WSe₂ waveguide-integrated photodetector. In particular, by introducing proximity screening by a nearby graphite layer to this structure, we prolong the hot-carrier cooling time, leading to an enhanced photoresponse. We characterize the cooling dynamics under continuous-wave laser excitation by employing a photomixing technique, revealing an increase in the cooling time by up to a factor of four. Direct photoresponse measurements show that the internal photoresponsivity improves by approximately 50%. Together, these results demonstrate the potential of proximity screening

*Corresponding author: k.j.tielrooij@tue.nl

to enhance the performance of graphene-based photodetectors on an integrated photonics platform.

Keywords: graphene, photodetection, cooling dynamics, proximity screening

1 Introduction

Photodetectors facilitate the conversion of optical signals into electrical signals, a capability widely required in both long-haul optical communication systems and short-range data center applications. Graphene is a promising material for photodetection owing to its zero bandgap, high carrier mobility, low electronic heat capacity [1, 2, 3], and its ability to generate a direct electron-heat-driven photovoltage signal without requiring an external bias [4, 5]. This strongly reduces the dark current and removes the need for a transimpedance amplifier [6, 7, 8, 9]. Graphene-based photodetectors also offer extremely fast operation, up to hundreds of GHz [10]. However, in order to compete with commercial photodetectors, such as those based on germanium, it is necessary for graphene-based photodetectors to increase their photoresponsivity [11].

To enhance the photoresponsivity of graphene photodetectors, several approaches have been explored, mostly aimed at increasing light absorption in graphene, including optical ring resonators [7] and plasmonic nanostructures [9]. Alternatively, it has recently been proposed that slower cooling of hot carriers, tailored via proximity screening, can lead to an increased photoresponse, as it leads to an increased average carrier temperature [12]. The resulting steeper temperature gradients enhance the thermally driven transport of photo-generated carriers, thereby strengthening the photoresponse. This strategy of increasing the photoresponse through slower hot carrier cooling requires control over the cooling dynamics, which have been reviewed in Ref. [13].

Recent work demonstrated that high-quality WSe₂-encapsulated graphene exhibits longer cooling times than hexagonal boron nitride (hBN)-encapsulated graphene, with the cooling dynamics ultimately limited by the emission of optical phonons [14]. In this scenario, rapid carrier-carrier scattering efficiently re-thermalizes the electronic system, maintaining relatively fast optical-phonon-mediated cooling that occurs on a picosecond timescale [14]. Motivated by very recent work demonstrating the slowing of cooling dynamics in a high-permittivity environment [12], enhanced responsivities in photodetectors based on WSe₂-encapsulated graphene [15], and enhanced

quantum mobilities due to proximity screening [16], further improvements to the photoresponse seem to be attainable.

These encouraging developments make an experimental demonstration of proximity screening effects in graphene photodetectors integrated on a silicon photonic platform highly desirable, in order to demonstrate relevance in real-world applications. However, until now, this has been lacking. In this work, we investigate the influence of proximity screening from a nearby graphite layer on a WSe₂–graphene–WSe₂ waveguide-integrated photodetector. We experimentally compare the cooling dynamics and photoresponse of the exact same device before and after placing the graphite layer, corresponding to the situation without and with proximity screening, respectively. Since the photodetectors of datacommunication and telecommunication applications operate under low-power illumination, we characterize the cooling dynamics using a continuous-wave (CW)-laser-based photomixing technique, based on Ref. [17], rather than measurements with ultrashort pulses, as these correspond to high peak powers [13]. Our results show that the introduction of proximity screening leads to an increase in the cooling time by a factor of 2–4, and a 1.5-fold enhancement in the graphene photoresponsivity. This shows that engineering the hot carrier cooling dynamics is indeed a promising strategy for enhancing the performance of graphene-based, silicon-photonics-integrated photodetectors.

2 Results

2.1 WSe₂-graphene-WSe₂ waveguide photodetector

Figure 1a shows the schematic of our device, a WSe₂-graphene-WSe₂ waveguide-integrated photodetector with graphite screening layer on top. We prepared a stack of WSe₂-graphene-WSe₂, which we dry-transferred to a silicon optical waveguide designed for operation at the telecom wavelength 1550 nm, forming the channel. The silicon optical waveguide has dimensions of 450 nm × 220 nm and is covered by a few-nanometer-thick planarized oxide top cladding. We use WSe₂ as the encapsulating material, rather than hBN, because it suppresses hyperbolic phonon mediated cooling, making intrinsic optical phonon cooling the dominant relaxation channel [14, 18, 19]. The graphene is exfoliated from high-quality crystals, to minimize disorder and defects, thereby suppressing supercollision cooling [20, 21]. The dry-transfer process [22], assisted by polycarbonate/PDMS stamps, sequentially picked up the flakes to assemble the stack, which was then transferred onto the silicon waveguide. Following the dry-transfer process, plasma etching and metal deposition were performed to

form edge contacts [23] to the WSe₂-encapsulated graphene, completing the device for the unscreened case. For the screened case, a graphite layer was deposited on top through an additional dry-transfer step.

Figure 1b shows the top view of the device in the unscreened case, where the stack length is $L_{\text{stack}} = 40 \mu\text{m}$. A longer stack leads to increased absorption, yet not necessarily a stronger photoresponse. Figure 1c presents the top view of the screened configuration, in which the graphite screening layer, which has a length of $L_{\text{graphite}} = 25 \mu\text{m}$, is placed on top. Light propagates along the z -direction within the silicon waveguide. As it passes through the stacked region, the evanescent field overlaps with the graphene layer and is partially absorbed, generating a photoresponse. The cross section of the optical field profile in the waveguide is shown in Fig. 1d, while Fig. 1e shows the optical field in the graphene channel, highlighting a minimal difference between the unscreened and screened cases. The simulated optical mode profile changes only weakly due to the graphite, indicating that the main role of the graphite layer is proximity screening.

The concept of proximity screening is illustrated in Fig. 1(f–g), for the example of an electron and a hole, where the field lines—including those in between the electron and hole—are affected by the presence of the graphite layer. The Coulomb interaction among carriers is given by $V(q) = e^2/(2\epsilon q)$ (unscreened) and $V(q) = (1 - e^{-2qd}) \cdot e^2/(2\epsilon q)$ (screened), where q is the carrier momentum, e denotes the elementary charge, ϵ represents the permittivity, and d is the distance between graphene and graphite. The presence of nearby graphite imposes a small d , which suppresses the Coulomb interaction via proximity screening. This screening weakens carrier–carrier scattering in graphene, which in turn slows down the re-thermalization processes associated with optical phonon cooling. As a result, the cooling time of photo-generated hot carriers is prolonged, as shown in Ref. [12]. Under steady-state optical excitation, this leads to a higher carrier temperature, enhancing the electron-heat-driven photovoltages.

To verify this proximity screening effect on the cooling dynamics and the photoresponse, we characterized the cooling time on the same device for both the unscreened and screened cases using a CW laser technique, thereby closely mimicking realistic datacommunication and telecommunication operating conditions. We also performed photoresponse measurements for both the unscreened and screened cases to evaluate if the prolonged cooling time leads to enhanced performance in terms of the responsivity.

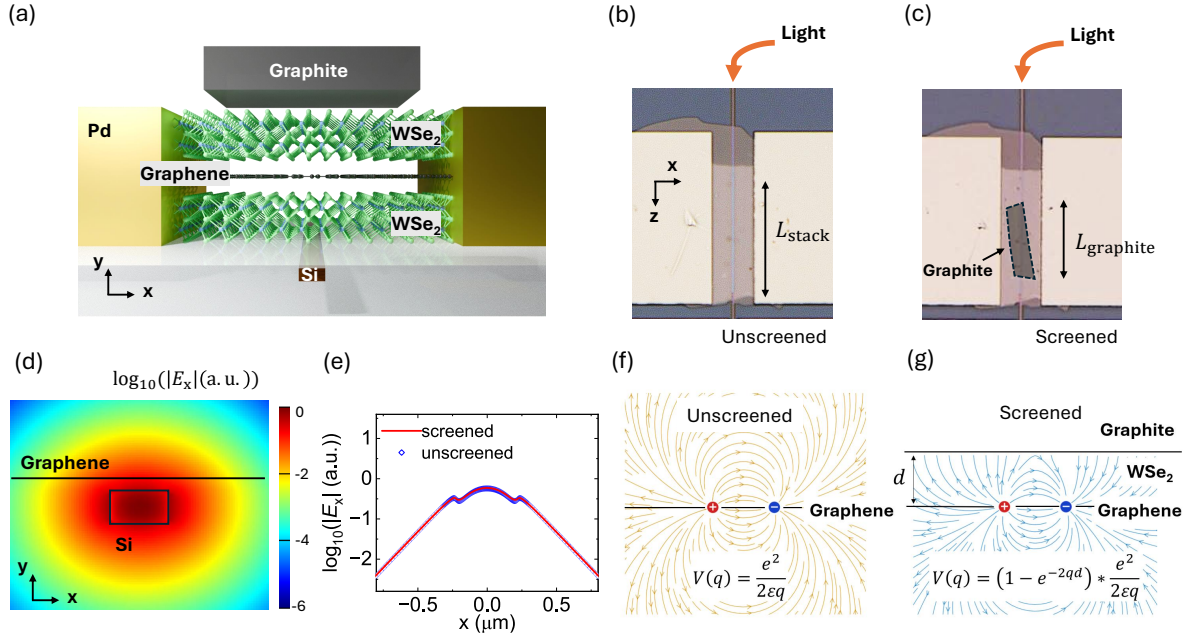


Figure 1: (a) Schematic of the cross section of the measured device, consisting of WSe₂-encapsulated graphene placed on a silicon waveguide, and a graphite screening layer on top. (b–c) Top view of the WSe₂–graphene–WSe₂ waveguide photodetector for the unscreened (b) and screened (c) cases. (d) Cross section of the optical field profile in the waveguide. (e) The optical field in graphene for the unscreened and screened cases. (f–g) Illustration of the physical mechanism behind the proximity screening effect, for the example of an electron and a hole, for the unscreened (f) and screened (g) case. The field lines are affected by the graphite layer, suppressing the strength of the carrier–carrier interaction. The equations describe the Coulomb interaction among carriers in the (un)screened case, where q is the carrier momentum, e denotes the elementary charge, ϵ represents the permittivity, and d is the distance between graphene and graphite.

2.2 Cooling time characterization

We study the hot-carrier cooling dynamics using heterodyne photomixing (see Fig. 2a). Two continuous-wave distributed feedback (DFB) lasers with a tunable frequency mix to form a beat note, which is then coupled into the optical waveguide of the graphene device through a grating coupler. The optical beat note periodically modulates the absorbed power, causing the carrier temperature to oscillate at the beat frequency, which is given by the relative frequency detuning of the two DFB lasers. Because the photovoltage depends nonlinearly on the carrier temperature, this produces a time-averaged beating photovoltage, which we measure using a lock-in amplifier. At low beat frequencies, the carriers can follow the modulation, whereas at high beat frequencies they cannot respond fast enough, causing the mixing signal to roll off. The cooling time is extracted from this frequency-dependent roll-off [17]. This continuous-wave method probes the device in a low- ΔT regime, where the electron temperature does not increase much beyond the lattice temperature, closer to realistic device operating conditions. It therefore provides direct access to the intrinsic carrier cooling dynamics without strongly perturbing the electron distribution.

Figure 2b shows the normalized heterodyne photovoltage response as a function of beat frequency for the device with and without graphite screening. The solid lines are descriptions with a Lorentzian function of the frequency-domain response of the beating photovoltage, where the width is inversely proportional to the cooling time [17] (see also Supplementary Note 2). The data shown in Fig. 2b correspond to the same absorbed power of $\approx 70 \mu\text{W}$ in both the unscreened and screened cases. At this power, the extracted cooling time increases from $\tau \approx 1.2 \text{ ps}$ in the unscreened case to $\tau \approx 2.2 \text{ ps}$ in the screened case. In Supplementary Note 4, we show a detailed simulation of the full experiment, relating the obtained cooling time from the frequency roll-off to a microscopic cooling time that serves as input to the simulation of the experiment. We find that the photomixing technique tends to somewhat underestimate the cooling time, in contrast to time-resolved photocurrent measurements, which tend to somewhat overestimate the cooling time. This means that the cooling times that we obtain here are lower bounds.

Figure 2c summarizes the extracted cooling times as a function of the absorbed optical power in graphene. The absorbed power is quantified by accounting for the excess waveguide propagation losses (see Supplementary Note 3). These losses are higher in the screened case than in the unscreened case, which is due to optical absorption in the graphite screening layer. The

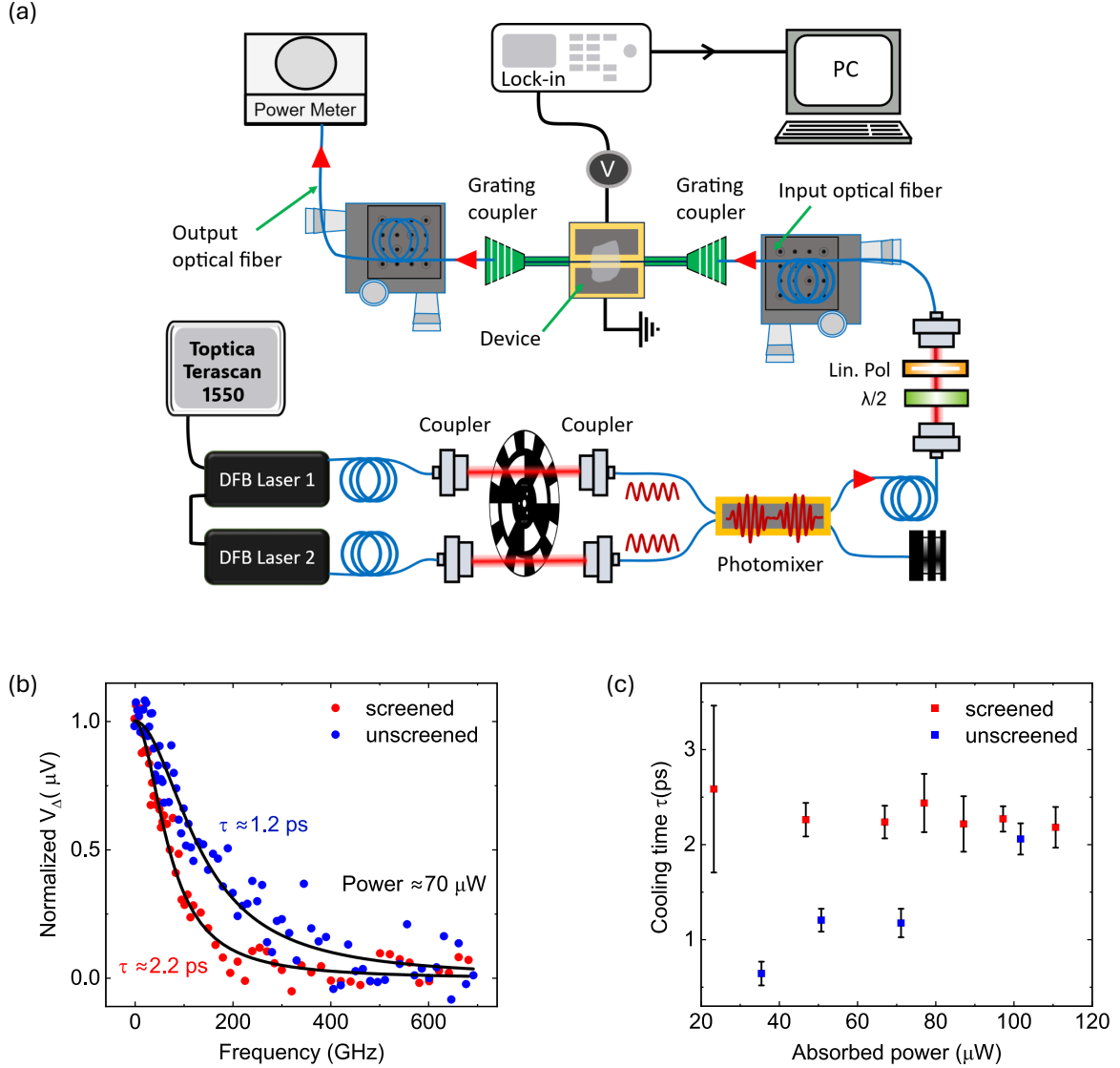


Figure 2: (a) Schematic of the experimental setup. Two continuous-wave distributed feedback lasers with a tunable difference frequency are combined and coupled into the waveguide of the device via grating couplers. The incident light is mechanically modulated with a chopper, and the resulting mixing photovoltage (V_{Δ}) is detected using a lock-in amplifier. (b) Normalized, background-subtracted photovoltage response as a function of the heterodyne beat frequency. The data points represent the measured response for the device in the unscreened (blue circles) and screened (red circles) cases. The solid lines indicate Lorentzian descriptions used to extract the hot-carrier cooling time τ , yielding $\tau \approx 1.2$ ps and $\tau \approx 2.2$ ps for the unscreened and screened cases, respectively, at an absorbed power of ≈ 70 μ W. (c) Measured hot-carrier cooling time τ as a function of absorbed power for the device in the unscreened (blue squares) and screened (red squares) cases. The screened device shows a longer and more stable cooling time over the measured power range. The error bars are based on multiple measurements as a function of difference frequency and represent the 68% confidence interval.

screened device exhibits a longer cooling time than the unscreened device over the measured power range, and its cooling time remains nearly independent of power. This contrasts with the clear power dependence of τ observed in the unscreened case. We attribute the longer cooling time in the screened case to the proximity screening of carrier–carrier interactions, as proposed in Ref. [12]. This weakens carrier–carrier scattering and reduces the efficiency of electronic re-thermalization within the optical-phonon-mediated cooling dynamics, thereby increasing the effective hot-carrier cooling time. In contrast, in the unscreened case, electronic re-thermalization remains efficient, enabling optical-phonon emission and the onset of a hot-phonon bottleneck, as shown in Ref. [14], which leads to a stronger power dependence of the cooling time.

2.3 Photoresponse

With the cooling time shown to increase after adding a graphite screening layer, we next compare the photoresponse of the device before and after adding the screening layer. As shown in Fig. 3a, the device with the graphite screening layer exhibits a higher photovoltage for a given absorbed power, demonstrating a clear improvement of internal photoresponsivity. In both cases, the photovoltage increases monotonically with absorbed power, with no clear saturation over the measured range.

Figure 3b shows the measured improvement factor, which is approximately 1.5. This improvement factor can be explained by using the measured cooling-time data as input for simulations based on the photothermoelectric effect driven by hot carriers in graphene [5, 13, 24] (see Supplementary Note 4). It confirms that the measured cooling time data and the measured photoresponse are consistent with our hypothesis that proximity screening suppresses the efficiency of cooling channels, effectively “trapping” heat within the electronic system.

3 Discussion

Having demonstrated slower cooling and an increased photoresponse enabled by screening of carrier–carrier interactions by a nearby graphite layer, we now discuss strategies to further improve device performance by exploiting the proximity screening effect. One approach to increase the screening of carrier–carrier scattering is to place the graphite screening layer very close to the graphene channel, on the order of ~ 1 nm. Such extremely close proximity screening configurations have been studied in studies aimed at (hydrodynamic) charge transport [16, 25]; however, it is not yet clear to

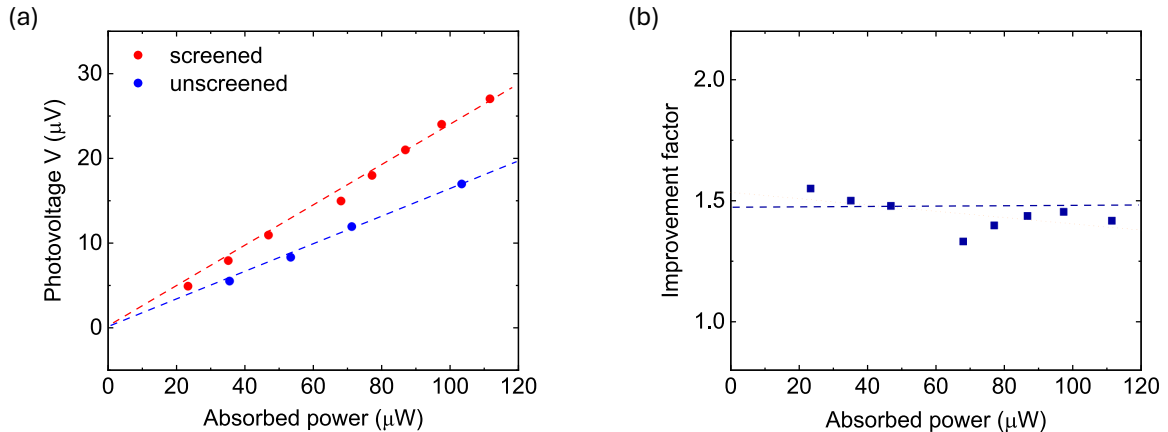


Figure 3: (a) Measured photovoltage as a function of absorbed power for the device in the unscreened (blue circles) and screened (red circles) cases, with dashed lines indicating linear fits. (b) Improvement factor as a function of absorbed power, with the dashed line indicating the average value of ≈ 1.5 .

what extent this enhanced screening would influence the carrier cooling time and the photoresponse.

To estimate this, we refer to very recent work that examined the impact of dielectric screening on cooling times in graphene [12]. For pure dielectric screening, numerical simulations of the cooling dynamics reveal that the cooling time scales approximately linearly with permittivity, $\tau \propto \epsilon$ (see Supplementary Note 5). In the presence of proximity screening and for small graphene–graphite distance d , the Coulomb interaction $V(q) \approx e^2 d/\epsilon$, such that the cooling time scales as $\tau \propto 1/d$.

In the limit of a monolayer WSe_2 spacer, the distance between graphene and graphite is $d \approx 1.3 \text{ nm}$, determined by the monolayer WSe_2 thickness and the van der Waals spacing. This means that we could expect an additional $4.7\times$ enhancement of the cooling time beyond our measured results for which $d \approx 6.1 \text{ nm}$, yielding approximately a $12\times$ enhancement of cooling time compared to the unscreened case. If we assume a photodetector operating under the photo-thermoelectric effect in graphene, where the photovoltage scales as the square root of the cooling time [5, 12, 24], this would correspond to a $3.5\times$ enhancement of the photoresponse.

4 Conclusions

In this work, we demonstrate that proximity screening can prolong the cooling time of hot carriers in graphene, leading to improved internal photoresponsivity. Specifically, by introducing a graphite screening layer at

a distance of 6.1 nm from graphene, the carrier cooling time is prolonged by up to a factor of four at low optical powers, resulting in a $\sim 50\%$ enhancement of the intrinsic photoresponse. Further improvement in responsivity with an extremely nearby proximity layer is expected, which is possibly enough to outcompete several competing receiver technology platforms. In addition to exploring extremely proximate screening layers, future work should address the challenge of maintaining optimal absorption in the graphene channel. The fact that our device was fabricated on a standard waveguide platform and characterized using a CW-laser-based photomixing technique highlights the potential for datacommunication and telecommunication applications.

Acknowledgments

This work was funded by FLAG-ERA project “ENPHOCAL”, by MICIN with No. PCI2021-122101-2A (Spain) and FWO SBO with No. S008421N (Belgium). The ICN2 is supported by the Severo Ochoa Centres of Excellence programme, Grant CEX2021-001214-S, funded by MCIU/AEI/10.13039.50110001 K.-J.T. acknowledges funding from the European Union’s Horizon 2020 research and innovation program under Grant Agreement No. 101125457 (ERC CoG “EQUATE”).

Author contributions

Y.H. designed and fabricated the device. A.N. performed the measurements. Y.H., A.N., and K.-J.T. interpreted the results, with input from D.V.T. and C.H. A.W.C. and A.P. performed the simulations of the photodetector response and cooling dynamics, with input from K.-J.T. F.L. performed the simulations of the photomixing experiment. B.L., S.B., H.I.W., and M.D. provided input for the fabrication and device aspects. Y.H., A.N., A.W.C., D.V.T., and K.-J.T. wrote the manuscript, with input from all authors. D.V.T., C.H., and K.-J.T. supervised the work. K.-J.T. conceived the idea and coordinated the project.

Data availability

All data used to generate the figures in this study are available from the corresponding author on reasonable request.

References

- [1] Deji Akinwande et al. “Graphene and two-dimensional materials for silicon technology”. In: *Nature* 573.7775 (2019), pp. 507–518. URL: [10.1038/s41586-019-1573-9](https://doi.org/10.1038/s41586-019-1573-9).
- [2] Muhammad A. Aamir et al. “Ultrasensitive calorimetric measurements of the electronic heat capacity of graphene”. In: *Nano Letters* 21.12 (2021), pp. 5330–5337. DOI: [10.1021/acs.nanolett.1c01553](https://doi.org/10.1021/acs.nanolett.1c01553). URL: <https://doi.org/10.1021/acs.nanolett.1c01553>.
- [3] Andreas Pospischil et al. “CMOS-compatible graphene photodetector covering all optical communication bands”. In: *Nature Photonics* 7.11 (2013), pp. 892–896. DOI: [10.1038/nphoton.2013.253](https://doi.org/10.1038/nphoton.2013.253). URL: <https://doi.org/10.1038/nphoton.2013.253>.
- [4] Nathaniel M. Gabor et al. “Hot carrier–assisted intrinsic photoreponse in graphene”. In: *Science* 334.6056 (2011), pp. 648–652. DOI: [10.1126/science.1211384](https://doi.org/10.1126/science.1211384). URL: <https://www.science.org/doi/abs/10.1126/science.1211384>.
- [5] Justin C. W. Song et al. “Hot carrier transport and photocurrent response in graphene”. In: *Nano Letters* 11.11 (2011), pp. 4688–4692. DOI: [10.1021/nl202318u](https://doi.org/10.1021/nl202318u). URL: <https://doi.org/10.1021/nl202318u>.
- [6] S. Marconi et al. “Photo thermal effect graphene detector featuring 105 Gbit s⁻¹ NRZ and 120 Gbit s⁻¹ PAM4 direct detection”. In: *Nature Communications* 12.1 (2021), p. 806. DOI: [10.1038/s41467-021-21137-z](https://doi.org/10.1038/s41467-021-21137-z). URL: <https://doi.org/10.1038/s41467-021-21137-z>.
- [7] S. Schuler et al. “High-responsivity graphene photodetectors integrated on silicon microring resonators”. In: *Nature Communications* 12.1 (2021), p. 3733. DOI: [10.1038/s41467-021-23436-x](https://doi.org/10.1038/s41467-021-23436-x). URL: <https://doi.org/10.1038/s41467-021-23436-x>.
- [8] Laiwen Yu et al. “High-bandwidth zero-biased waveguide-integrated p-n homojunction graphene photodetectors on silicon for a wavelength band of 1.55 μm and beyond”. In: *ACS Photonics* 10.10 (2023), pp. 3621–3628. DOI: [10.1021/acsp Photonics.3c00688](https://doi.org/10.1021/acsp Photonics.3c00688). URL: <https://doi.org/10.1021/acsp Photonics.3c00688>.
- [9] Jakob E. Muench et al. “Waveguide-integrated, plasmonic enhanced graphene photodetectors”. In: *Nano Letters* 19.11 (2019), pp. 7632–7644. DOI: [10.1021/acs.nanolett.9b02238](https://doi.org/10.1021/acs.nanolett.9b02238). URL: <https://doi.org/10.1021/acs.nanolett.9b02238>.

- [10] Stefan M. Koepfli, Michael Baumann, Robin Gadola, et al. “Controlling photothermoelectric directional photocurrents in graphene with over 400 GHz bandwidth”. In: *Nature Communications* 15 (2024), p. 7351. DOI: [10.1038/s41467-024-51599-w](https://doi.org/10.1038/s41467-024-51599-w).
- [11] S. Lischke et al. “Ultra-fast germanium photodiode with 3-dB bandwidth of 265 GHz”. In: *Nature Photonics* 15.12 (2021), pp. 925–931. DOI: [10.1038/s41566-021-00893-w](https://doi.org/10.1038/s41566-021-00893-w). URL: <https://doi.org/10.1038/s41566-021-00893-w>.
- [12] Hai I. Wang et al. *Dielectric control of ultrafast carrier dynamics and transport in graphene*. arXiv: [2604.00217](https://arxiv.org/abs/2604.00217).
- [13] Mathieu Massicotte et al. “Hot carriers in graphene – fundamentals and applications”. In: *Nanoscale* 13 (18 2021), pp. 8376–8411. DOI: [10.1039/D0NR09166A](https://doi.org/10.1039/D0NR09166A). URL: <http://dx.doi.org/10.1039/D0NR09166A>.
- [14] Eva A. A. Pogna et al. “Hot-carrier cooling in high-quality graphene is intrinsically limited by optical phonons”. In: *ACS Nano* 15.7 (2021). PMID: 34139125, pp. 11285–11295. DOI: [10.1021/acsnano.0c10864](https://doi.org/10.1021/acsnano.0c10864). URL: <https://doi.org/10.1021/acsnano.0c10864>.
- [15] Karuppasamy Soundarapandian. “to be published”. In: ().
- [16] Daniil Domaretskiy et al. “Proximity screening greatly enhances electronic quality of graphene”. In: *Nature* 644.8077 (2025), pp. 646–651. DOI: [10.1038/s41586-025-09386-0](https://doi.org/10.1038/s41586-025-09386-0). URL: <https://doi.org/10.1038/s41586-025-09386-0>.
- [17] M. Mehdi Jadidi et al. “Tunable ultrafast thermal relaxation in graphene measured by continuous-wave photomixing”. In: *Phys. Rev. Lett.* 117 (25 Dec. 2016), p. 257401. DOI: [10.1103/PhysRevLett.117.257401](https://doi.org/10.1103/PhysRevLett.117.257401). URL: <https://link.aps.org/doi/10.1103/PhysRevLett.117.257401>.
- [18] Alessandro Principi et al. “Super-Planckian electron cooling in a van der Waals stack”. In: *Physical Review Letters* 118.12 (2017), p. 126804. DOI: [10.1103/PhysRevLett.118.126804](https://doi.org/10.1103/PhysRevLett.118.126804). URL: <https://doi.org/10.1103/PhysRevLett.118.126804>.
- [19] Klaas-Jan Tielrooij et al. “Out-of-plane heat transfer in van der Waals stacks through electron–hyperbolic phonon coupling”. In: *Nature Nanotechnology* 13.1 (2018), pp. 41–46. DOI: [10.1038/s41565-017-0008-8](https://doi.org/10.1038/s41565-017-0008-8). URL: <https://doi.org/10.1038/s41565-017-0008-8>.

- [20] Justin C. W. Song, Michael Y. Reizer, and Leonid S. Levitov. “Disorder-assisted electron-phonon scattering and cooling pathways in graphene”. In: *Phys. Rev. Lett.* 109 (10 Sept. 2012), p. 106602. DOI: [10.1103/PhysRevLett.109.106602](https://doi.org/10.1103/PhysRevLett.109.106602). URL: <https://link.aps.org/doi/10.1103/PhysRevLett.109.106602>.
- [21] A. C. Betz et al. “Supercollision cooling in undoped graphene”. In: *Nature Physics* 9.2 (2013), pp. 109–112. ISSN: 1745-2481. DOI: [10.1038/nphys2494](https://doi.org/10.1038/nphys2494). URL: <https://doi.org/10.1038/nphys2494>.
- [22] Kei Kinoshita et al. “Dry release transfer of graphene and few-layer h-BN by utilizing thermoplasticity of polypropylene carbonate”. In: *npj 2D Materials and Applications* 3.1 (2019), p. 22. ISSN: 2397-7132. DOI: [10.1038/s41699-019-0104-8](https://doi.org/10.1038/s41699-019-0104-8). URL: <https://doi.org/10.1038/s41699-019-0104-8>.
- [23] L. Wang et al. “One-dimensional electrical contact to a two-dimensional material”. In: *Science* 342.6158 (2013), pp. 614–617. DOI: [10.1126/science.1244358](https://doi.org/10.1126/science.1244358). eprint: <https://www.science.org/doi/pdf/10.1126/science.1244358>. URL: <https://www.science.org/doi/abs/10.1126/science.1244358>.
- [24] Aleandro Antidormi and Aron W. Cummings. “Optimizing the photothermoelectric effect in graphene”. In: *Physical Review Applied* 15.5 (2021), p. 054049. DOI: [10.1103/PhysRevApplied.15.054049](https://doi.org/10.1103/PhysRevApplied.15.054049). URL: <https://doi.org/10.1103/PhysRevApplied.15.054049>.
- [25] M. Kim et al. “Control of electron-electron interaction in graphene by proximity screening”. In: *Nature Communications* 11.1 (2020), p. 2339. DOI: [10.1038/s41467-020-15829-1](https://doi.org/10.1038/s41467-020-15829-1). URL: <https://doi.org/10.1038/s41467-020-15829-1>.

Supplementary Information

Note 1. Device Fabrication

AFM data of flakes

Monolayer graphene and few-layer WSe₂ flakes (top and bottom layers) were mechanically exfoliated from bulk crystals. Optical microscope images of these flakes are presented in Fig. S1a–c, corresponding to monolayer graphene, the top WSe₂ few-layer flake, and the bottom WSe₂ few-layer flake, respectively. Atomic force microscopy (AFM) measurements of the WSe₂ layers are shown in Fig. S1d and Fig. S1e for the top and bottom layers, respectively. The extracted thicknesses are approximately 5.5 nm for the top layer and 5.0 nm for the bottom layer. The AFM height measurement of graphene is not included, as the standard tapping mode used in our AFM setup does not provide reliable thickness determination for monolayer graphene.

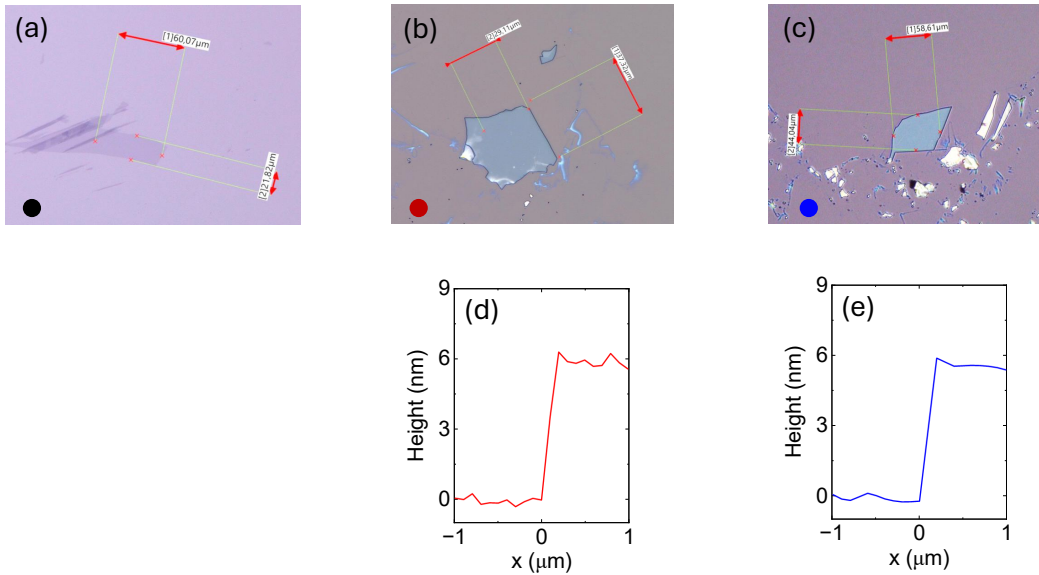


Figure S1: Optical microscope images of (a) monolayer graphene, (b) top WSe₂ few-layer flake, and (c) bottom WSe₂ few-layer flake. (d, e) Atomic force microscopy (AFM) height profiles of the top and bottom WSe₂ layers, respectively.

Raman of WSe₂-graphene-WSe₂

To verify the monolayer nature and quality of WSe₂-encapsulated graphene, a Raman measurement was conducted. The Raman check point and the corresponding Raman spectrum are shown in Fig. S2a and Fig. S2b, respectively. The full width at half maximum (FWHM) of the 2D peak is 20 cm⁻¹, indicating low disorder in the encapsulated graphene and—as a result—suppressed supercollision cooling [1].

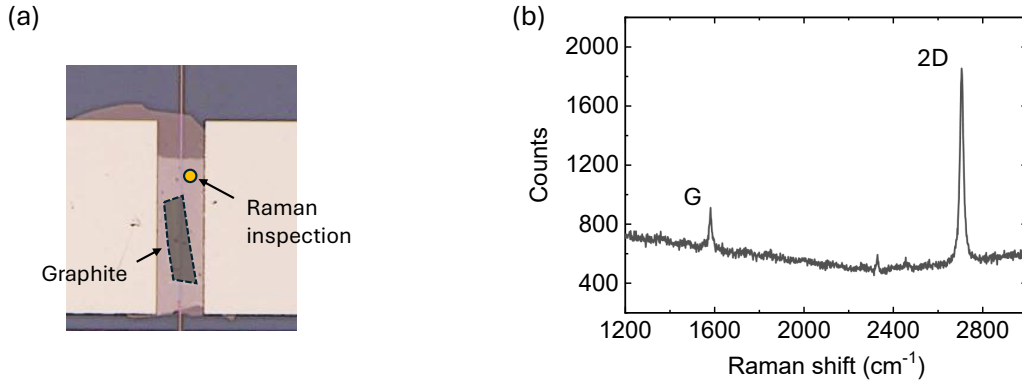


Figure S2: (a) Microscope image and (b) Raman spectrum of the spare WSe₂-graphene-WSe₂ stack.

Note 2. Photomixing measurement

Figure S3 shows the heterodyne photomixing measurements of the normalized photovoltage V_{Δ} as a function of beat frequency for both the un-screened (Fig. S3a) and proximity-screened (Fig. S3b) devices, recorded over a range of input optical powers. The solid symbols represent the measured data, while the solid lines are fits used to extract the hot-carrier cooling time τ .

The observed frequency dependence arises from the finite cooling time of hot carriers. Within the thermal model, the response follows a Lorentzian form in angular frequency [2],

$$\frac{\gamma^2}{\omega^2 + \gamma^2}, \quad (\text{S1})$$

where $\omega = \omega_1 - \omega_2$ is the optical beat frequency and $\gamma = 1/\tau$ is the carrier cooling rate. This explicitly shows that the frequency-dependent

photovoltage is governed by a Lorentzian response, with the width set by the cooling dynamics.

Experimentally, the data are analyzed as a function of the linear frequency $f = \omega/2\pi$. In this representation, the photovoltage is described by

$$V_{\Delta}(f) = V + \frac{A}{1 + (2\pi f\tau)^2}, \quad (\text{S2})$$

where V is the high-frequency asymptotic value and A is the amplitude of the frequency-dependent contribution. Since only positive beat frequencies ($f \geq 0$) are experimentally accessible, the measured response corresponds to one half of a symmetric Lorentzian profile.

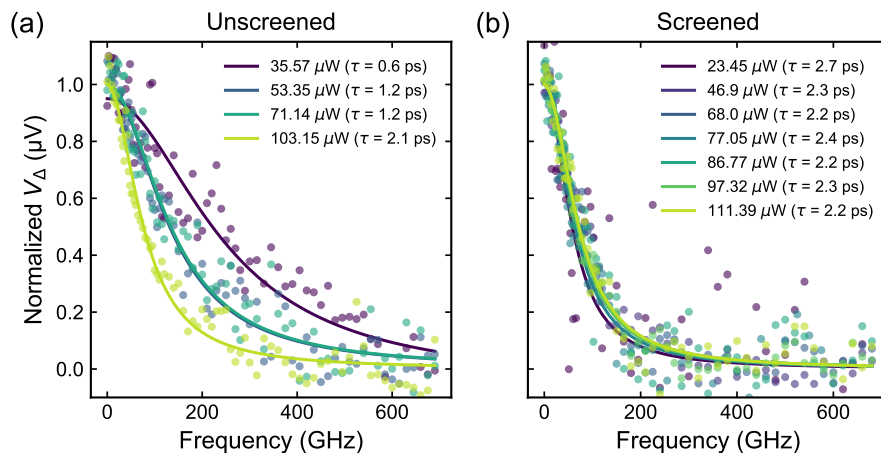


Figure S3: Normalized photovoltage V_{Δ} as a function of the heterodyne beat frequency for the (a) unscreened and (b) screened photodetector device. Data are plotted for various absorbed optical powers. Solid lines represent Lorentzian fits used to extract the hot-carrier cooling time τ .

The characteristic roll-off frequency in Fig. S3 reflects the inverse of the cooling time. In the unscreened device, the roll-off shifts significantly towards lower frequencies with increasing optical power, indicating a strong increase in τ . In contrast, the screened device (Fig. S3b) exhibits only a weak shift of the roll-off frequency, demonstrating that the cooling time remains nearly constant over the same power range. This difference directly highlights the suppression of power-dependent cooling dynamics in the presence of screening.

The heterodyne excitation is generated by two continuous-wave DFB lasers with angular frequencies ω_1 and ω_2 , producing a beat signal at $\omega = \omega_1 - \omega_2$. The resulting absorbed power is given by

$$P(t) = P_1 + P_2 + 2\sqrt{P_1 P_2} \cos(\omega t), \quad (\text{S3})$$

where P_1 and P_2 are the individual laser powers. Due to the nonlinear dependence of the photothermoelectric voltage on electron temperature, this

oscillating power leads to a rectified DC photovoltage. The finite carrier cooling time introduces a delayed response to this modulation, resulting in a suppression of the photovoltage at higher beat frequencies. This suppression follows the Lorentzian dependence described above, allowing direct extraction of τ from the frequency-dependent measurements.

Note 3. Graphene absorbed power

To quantify the optical power absorbed by graphene, the excess propagation loss from the stack and the graphite screening layer must be characterised. The procedure is described below.

Stack loss. The measured propagation loss for the unscreened case is $0.375 \text{ dB}/\mu\text{m}$, consisting of contributions from graphene absorption and excess loss. The excess loss arises from polymer residues introduced during the dry-transfer process and from optical scattering within the stack. The stack exhibits wrinkles, likely induced by lattice mismatch between WSe₂ and graphene [3], which contribute to the observed scattering loss.

Graphite loss. For the screened case, the additional optical loss of the graphite layer reduces the output power below the detection limit of our power meter, necessitating a separate loss characterisation. Figure S4a shows an optical microscope image of the loss test structure, a standard silicon waveguide at 1550 nm with a graphite layer ($L = 38 \mu\text{m}$) transferred on top. The silicon waveguide has a width of $w = 450 \text{ nm}$ and a height of $h = 220 \text{ nm}$; the SiO₂ spacer between graphite and waveguide is $t_0 = 10 \text{ nm}$ thick and the graphite thickness is $t_g = 12 \text{ nm}$. Figure S4b presents the measured transmission data, from which a propagation loss of $0.91 \text{ dB}/\mu\text{m}$ is extracted.

Absorbed power calculation. The graphite crystal used in this work is NGS Flaggy graphite [4], for which the refractive index is not readily available. To estimate it, we start from handbook values of highly oriented pyrolytic graphite (HOPG) from HQ Graphene [5]. At 1550 nm, the handbook values are $n = 2.5276$ and $k = 1.6688$, yielding a simulated propagation loss of $1.12 \text{ dB}/\mu\text{m}$, which exceeds the measured $0.91 \text{ dB}/\mu\text{m}$. To resolve this discrepancy we tune the Drude damping rate—preserving Kramers–Kronig relations—from $3.5 \times 10^{14} \text{ rad/s}$ to $2.45 \times 10^{14} \text{ rad/s}$, yielding revised constants $n = 2.38$ and $k = 1.23$ that reproduce the measured loss. The deviation from handbook values is attributed to differences in crystal quality between NGS Flaggy graphite and HOPG.

Incorporating these fitted optical constants into simulations of the screened WSe₂–graphene–WSe₂ waveguide yields an additional loss of $0.86 \text{ dB}/\mu\text{m}$ from the graphite layer. The total absorbed power in graphene is obtained

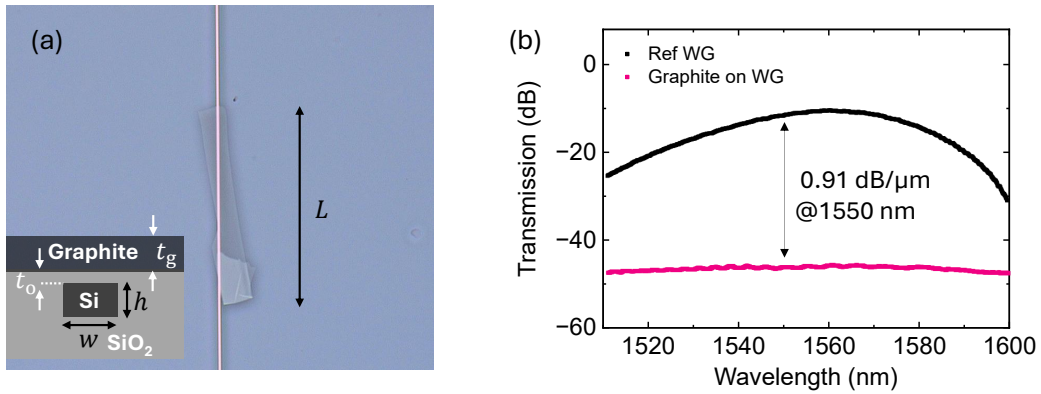


Figure S4: (a) Microscope image of the loss characterisation waveguide with graphite on it and (b) transmission spectra of the reference waveguide and the waveguide with graphite.

by integrating the absorption per length along the propagation direction (Fig. S6). The absorbed power per unit length for the unscreened and screened configurations is shown in Figs. S5a and S5b, respectively; in the screened case the graphite layer starts $7.5 \mu\text{m}$ into the stack region, causing the absorbed power to drop much more steeply. The photovoltages and cooling times in the main text are plotted against these integrated absorbed powers.

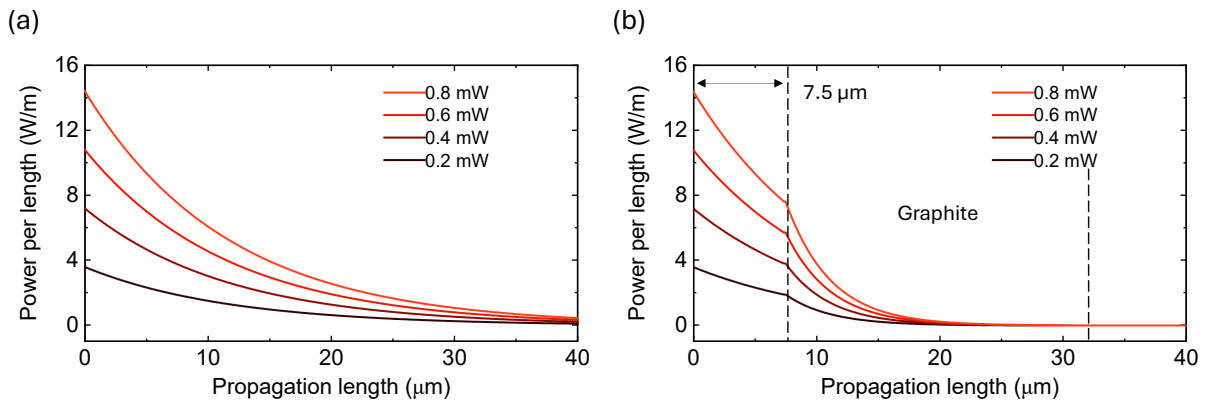


Figure S5: Absorbed power per unit length for the (a) unscreened and (b) screened cases at different input powers.

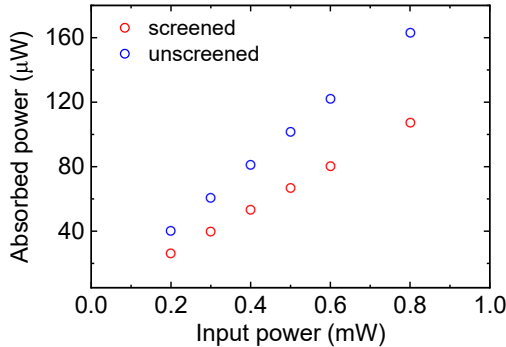


Figure S6: Total graphene absorbed power for different waveguide input powers.

Note 4. Simulation to recover the measured photovoltages using cooling time data

The measured photovoltages under zero bias are attributed to the photothermoelectric (PTE) effect, which arises from a photon-induced electron temperature gradient combined with asymmetric doping in the channel. Under zero-bias conditions, thermally driven carriers accumulate near the contacts, generating a voltage that enforces zero net current ($\nabla \cdot \mathbf{J} = 0$). This voltage corresponds to the PTE photovoltage.

Electron temperature profiles. To illustrate the effect of proximity screening on the PTE effect, we performed a heat transport simulation under CW laser input in steady state. The 1D heat transport equation is

$$C_e \frac{dT_e}{dt} = Q - C_e \frac{T_e - T_0}{\tau_{\text{cool}}} - K_e \frac{\partial^2 T_e}{\partial x^2}. \quad (\text{S4})$$

Note that the photovoltage simulations presented below use a 2D framework; the 1D case is shown here for clarity. A cross-sectional simulation provides the heating source profile (Fig. S7a). Figure S7b shows that increasing the cooling time from $\tau = 1.2$ ps to 2.3 ps raises the maximum electron temperature by approximately 20 K at an absorbed power of $60 \mu\text{W}$.

Modeling of waveguide-coupled photovoltages. Due to fabrication limitations the device lacks a well-defined electrostatic p-n junction. We therefore assume an effective asymmetric doping of ± 1.0 meV, which yields results consistent with the experimental data. The Dirac-point voltage is $U_{\text{Dirac}} = +140$ mV, corresponding to $E_F = -71.7$ meV at $U_{G1} = U_{G2} = 0$ V. The carrier mobility is assumed to be $10,000 \text{ cm}^2 \text{ V}^{-1} \text{ s}^{-1}$ based on the Raman characterisation in Note 1. The intrinsic doping level is consistent

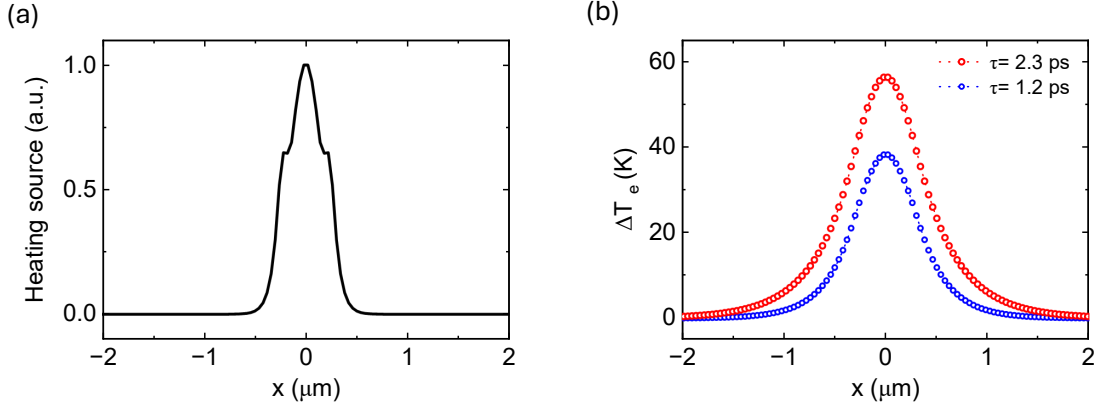


Figure S7: (a) Heating source and (b) electron temperature at the input cross section.

with the measured zero-gate channel resistance of $\approx 400 \Omega$ for both cases. The model includes the temperature-dependent Fermi-level shift due to elevated carrier temperature.

Photovoltage simulations are based on the 1D heat equation for the propagation-direction-averaged carrier-temperature profile [6, 7]:

$$\frac{\partial T_C(x, t)}{\partial t} = \frac{1}{C_e(x, t)} \frac{\partial}{\partial x} \left[\kappa_e(x, t) \frac{\partial T_C(x, t)}{\partial x} \right] + \frac{\dot{Q}_{\text{loss}}(x, t)}{C_e(x, t)} + \frac{p_{\text{abs}}(x, t)}{C_e(x, t)}, \quad (\text{S5})$$

where T_C is the carrier temperature, C_e is the electronic heat capacity per unit area, κ_e is the electronic thermal conductivity, \dot{Q}_{loss} is the carrier-cooling power density, and p_{abs} is the absorbed optical power density taken from Fig. S6.

The electronic heat capacity and thermal conductivity are calculated from graphene's finite-temperature carrier statistics and Boltzmann transport integrals [6, 7]. The thermal conductivity is obtained from the transport moments

$$K_j = \int (E - \mu)^j \Sigma(E) \left(-\frac{\partial f}{\partial E} \right) dE, \quad (\text{S6})$$

with

$$\Sigma(E) = \frac{e^2 v_F^2 \tau_p(E) D(E)}{2}, \quad D(E) = \frac{2|E|}{\pi(\hbar v_F)^2}. \quad (\text{S7})$$

The momentum relaxation time $\tau_p(E)$ includes acoustic-phonon and remote-impurity scattering [8].

Carrier cooling is modeled by a linear heat-loss term,

$$\dot{Q}_{\text{loss}}(x, t) = -C_e(x, t) \gamma_c [T_C(x, t) - T_L], \quad \gamma_c = \frac{1}{\tau_c}. \quad (\text{S8})$$

In the unscreened case a power-dependent τ_c is used; in the screened case a fixed τ_c is assumed. The lattice temperature T_L is kept constant. The heat equation is solved self-consistently with temperature-dependent transport coefficients using an implicit Crank–Nicolson finite-difference scheme [9].

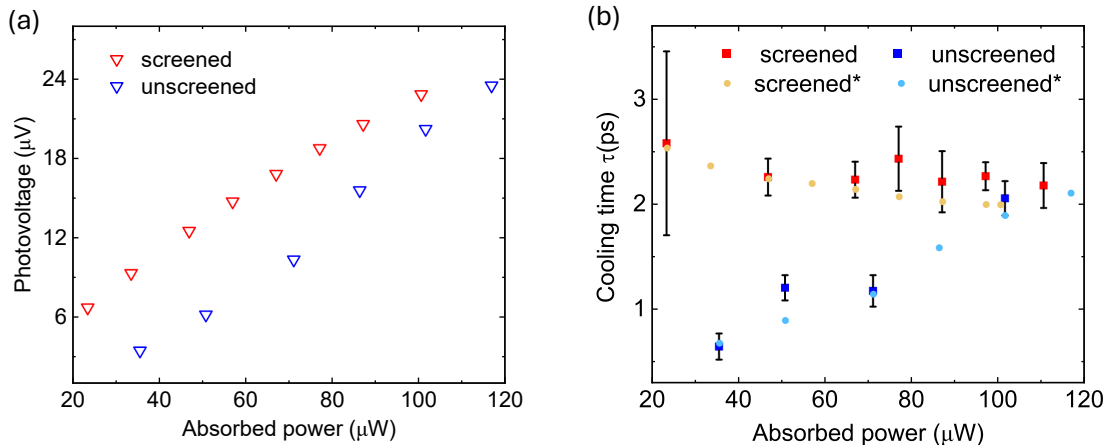


Figure S8: (a) Simulated photovoltages from the nonlinear photothermoelectric heat-transport model using $U_{\text{Dirac}} = +140 \text{ mV}$ ($E_F = -71.7 \text{ meV}$), asymmetric doping of $\pm 1.0 \text{ meV}$, and mobility $10,000 \text{ cm}^2 \text{ V}^{-1} \text{ s}^{-1}$. (b) Cooling times extracted from measured and simulated photomixing frequency roll-offs. Starred labels (“screened*”, “unscreened*”) denote cooling times extracted from simulated photomixing traces that include heat diffusion, after applying the same Lorentzian analysis as in Note 2.

Figure S8a shows the simulated photovoltages. The observed enhancement is reproduced in the intermediate power regime; deviations at low and high power arise from uncertainties in the effective absorbed power, the assumed Seebeck asymmetry, and the cooling-time data used as model input.

Figure S8b compares cooling times from measured and simulated photomixing traces. In all simulations, Eq. (S5) is solved in space and time including heat diffusion, and the resulting photovoltage is analyzed with the same Lorentzian fitting procedure as in Note 2. The starred data points represent the cooling times that the photomixing technique would extract from the simulated device response. The nonlinear heat-transport model captures the main trends of the measured cooling times and photovoltage response.

To further clarify the relation between the microscopic input cooling time and the photomixing-extracted cooling time, we performed an additional simulation with a fixed $\tau_c = 4 \text{ ps}$, using $U_{\text{G1}} = 0.3 \text{ V}$ and $U_{\text{G2}} = -0.3 \text{ V}$ to form a well-defined p–n junction, and a Gaussian optical heating profile with $D_{1/e^2} = 5 \mu\text{m}$.

As shown in Fig. S9, the photomixing-extracted cooling time can be systematically smaller than the microscopic input τ_c , with the underestima-

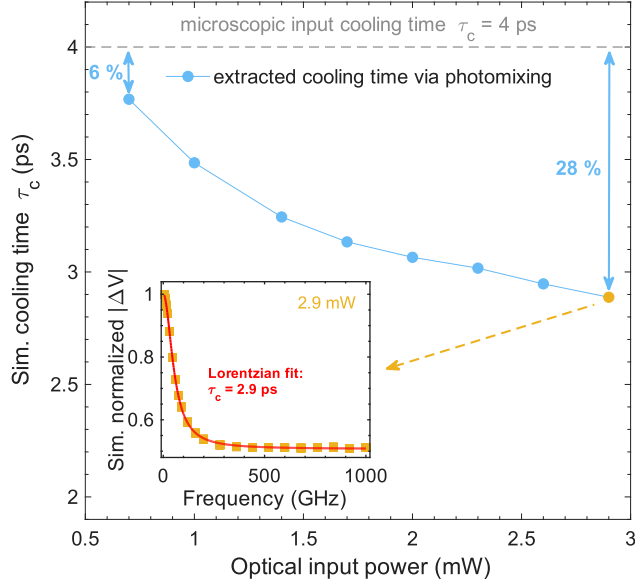


Figure S9: Simulated cooling-time extraction for a fixed microscopic input $\tau_c = 4$ ps. Dashed line marks the input value; percentages indicate the relative extraction error. Inset: normalized high-power photomixing roll-off with Lorentzian fit.

tion increasing at higher optical power. The deviation arises from the spatially extended, nonlinear nature of the heat-transport problem: lateral heat diffusion, temperature-dependent heat capacity and thermal conductance, and temperature-dependent chemical potential all modify the dynamic carrier-temperature profile beyond the approximations of simplified photomixing analyses [2]. This also suggests that experimental cooling times from such analyses may underestimate the true microscopic cooling time. A broader parameter-space study will be presented in a forthcoming publication.

Note 5. Cooling time of closer proximity screening

The Supplementary Material of Ref. [10] describes an approach for examining the cooling dynamics of hot carriers in graphene, arising from the combined effects of carrier-carrier scattering, optical phonon emission, and optical-to-acoustic phonon relaxation. Using that approach, we carried out simulations investigating the impact of dielectric screening. As shown in Fig. S10, the cooling time scales approximately linearly with permittivity. When placing a metal near the graphene layer, the Coulomb interaction becomes

$$V(q) = (1 - e^{-2qd}) \frac{e^2}{2\epsilon q}, \quad (\text{S9})$$

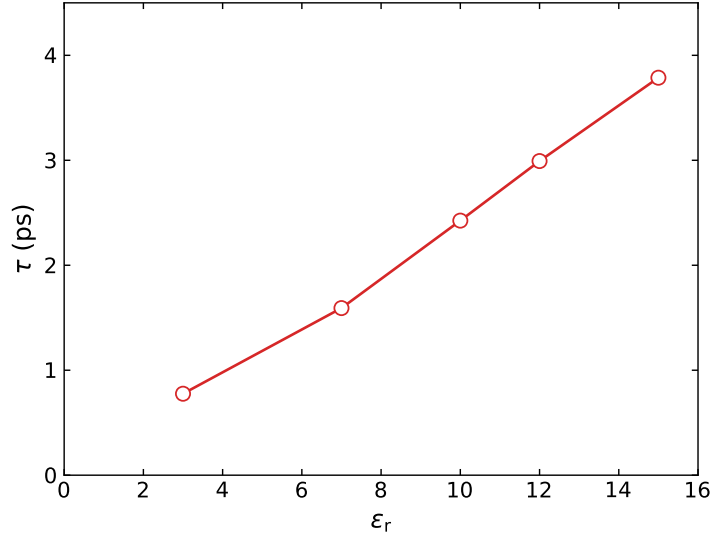


Figure S10: Hot-carrier cooling time as a function of surrounding permittivity, calculated using the approach of Ref. [10].

where d is the graphene–metal distance and q is the carrier momentum. In the limit of large d , the bare Coulomb potential is recovered. In the limit $qd \ll 1$, the interaction reduces to $V(q) = e^2d/\epsilon$, so that $\tau \propto 1/d$, analogous to the $\tau \propto \epsilon$ dependence seen above.

To verify that we operate in the regime $qd \ll 1$, we note that for clean WSe₂-encapsulated graphene the dominant cooling mechanism is optical phonon emission, followed by fast re-thermalization via carrier–carrier scattering [11]. At low optical powers the carrier distribution is near room temperature, so momentum transfers during re-thermalization are restricted to $q \lesssim k_B T / \hbar v_F \approx 1/25 \text{ nm}^{-1}$. For $d \leq 5.5 \text{ nm}$ we have $qd \ll 1$, confirming that $\tau \propto 1/d$ in our device geometry.

References

- [1] Justin C. W. Song, Michael Y. Reizer, and Leonid S. Levitov. “Disorder-assisted electron-phonon scattering and cooling pathways in graphene”. In: *Phys. Rev. Lett.* 109 (10 Sept. 2012), p. 106602. DOI: [10.1103/PhysRevLett.109.106602](https://doi.org/10.1103/PhysRevLett.109.106602). URL: <https://link.aps.org/doi/10.1103/PhysRevLett.109.106602>.
- [2] M. Mehdi Jadidi et al. “Tunable ultrafast thermal relaxation in graphene measured by continuous-wave photomixing”. In: *Phys. Rev. Lett.* 117 (25 Dec. 2016), p. 257401. DOI: [10.1103/PhysRevLett.117.257401](https://doi.org/10.1103/PhysRevLett.117.257401). URL: <https://link.aps.org/doi/10.1103/PhysRevLett.117.257401>.

- [3] Kyoungwan Kim et al. “Band alignment in WSe₂–graphene heterostructures”. In: *ACS Nano* 9.4 (2015). PMID: 25768037, pp. 4527–4532. DOI: [10.1021/acsnano.5b01114](https://doi.org/10.1021/acsnano.5b01114). eprint: <https://doi.org/10.1021/acsnano.5b01114>. URL: <https://doi.org/10.1021/acsnano.5b01114>.
- [4] NGS. “Flaggy Graphite”. In: (). URL: <https://www.graphit.de/en/graphite-info/flake-graphite-for-graphene/>.
- [5] Baokun Song et al. “Broadband optical properties of graphene and HOPG investigated by spectroscopic Mueller matrix ellipsometry”. In: *Applied Surface Science* 439 (2018), pp. 1079–1087. ISSN: 0169-4332. DOI: <https://doi.org/10.1016/j.apsusc.2018.01.051>. URL: <https://www.sciencedirect.com/science/article/pii/S0169433218300540>.
- [6] Aleandro Antidormi and Aron W. Cummings. “Optimizing the photothermoelectric effect in graphene”. In: *Physical Review Applied* 15.5 (2021), p. 054049. DOI: [10.1103/PhysRevApplied.15.054049](https://doi.org/10.1103/PhysRevApplied.15.054049). URL: <https://doi.org/10.1103/PhysRevApplied.15.054049>.
- [7] Mathieu Massicotte et al. “Hot carriers in graphene – fundamentals and applications”. In: *Nanoscale* 13 (18 2021), pp. 8376–8411. DOI: [10.1039/D0NR09166A](https://doi.org/10.1039/D0NR09166A). URL: <http://dx.doi.org/10.1039/D0NR09166A>.
- [8] R. S. Shishir et al. “Room temperature carrier transport in graphene”. In: *Journal of Computational Electronics* 8 (2009), pp. 43–50. DOI: [10.1007/s10825-009-0278-y](https://doi.org/10.1007/s10825-009-0278-y). URL: <https://doi.org/10.1007/s10825-009-0278-y>.
- [9] J. Crank and P. Nicolson. “A practical method for numerical evaluation of solutions of partial differential equations of the heat-conduction type”. In: *Proceedings of the Cambridge Philosophical Society* 43.1 (1947), pp. 50–67. DOI: [10.1017/S0305004100023197](https://doi.org/10.1017/S0305004100023197). URL: <https://doi.org/10.1017/S0305004100023197>.
- [10] Hai I. Wang et al. *Dielectric control of ultrafast carrier dynamics and transport in graphene*. arXiv: [2604.00217](https://arxiv.org/abs/2604.00217).
- [11] Eva A. A. Pogna et al. “Hot-carrier cooling in high-quality graphene is intrinsically limited by optical phonons”. In: *ACS Nano* 15.7 (2021). PMID: 34139125, pp. 11285–11295. DOI: [10.1021/acsnano.0c10864](https://doi.org/10.1021/acsnano.0c10864). URL: <https://doi.org/10.1021/acsnano.0c10864>.